Investigation of single- and double-Λ hypernuclei using a beyond-mean-field approach

Ji-Wei Cui (崔继伟),[1] Xian-Rong Zhou (周先荣),[2,*] Li-Xin Guo (郭立新),[1,†] and Hans-Josef Schulze[3]
[1]*School of Physics and Optoelectronic Engineering, Xidian University, Xi'an 710071, People's Republic of China*
[2]*Department of Physics, East China Normal University, Shanghai 200241, People's Republic of China*
[3]*INFN Sezione di Catania, Dipartimento di Fisica, Universitá di Catania, Via Santa Sofa 64, I-95123 Catania, Italy*
(Received 4 December 2016; published 27 February 2017)

A beyond-mean-field approach consisting of angular momentum projection techniques and generator coordinate method based on Skyrme–Hartree-Fock calculations is employed to investigate single- and double-Λ hypernuclear systems. The density-dependent $N\Lambda$ interactions derived from the Nijmegen soft-core potentials are used. Rotational energy spectra and electric-quadrupole transition strengths $B(E2)$ of the hypernuclei ${}^{13}_{\Lambda}$C, ${}^{14}_{\Lambda\Lambda}$C, ${}^{21}_{\Lambda}$Ne, and ${}^{22}_{\Lambda\Lambda}$Ne are presented and compared with those of the corresponding core nuclei ^{12}C and ^{20}Ne. The shrinkage effect of the Λs is demonstrated by the $B(E2)$ values, the charge radii, and the shape deformation β of the nuclear core. It is found that the reduction of the $B(E2)$ values in ${}^{13}_{\Lambda}$C and ${}^{14}_{\Lambda\Lambda}$C is mainly caused by the shrinkage of the charge radii of the nuclear cores, while the reduced shape deformations also play important roles; but the contrary is the case in ${}^{21}_{\Lambda}$Ne and ${}^{22}_{\Lambda\Lambda}$Ne. Comparison between this and other theoretical models are made, and the differences between them are illuminated.

DOI: 10.1103/PhysRevC.95.024323

I. INTRODUCTION

In the past half century, many experiments have been carried out to investigate the properties of Λ hypernuclei [1–3], and the observed low-lying energy spectra and electric multipole transition strengths provide useful information to study the impurity effect (shrinkage phenomenon [4] and spin splitting [5,6]) due to the Λ hyperon, which is deeply bound without Pauli blocking from the nucleons. In recent years, various events were also observed for double-Λ hypernuclei [7,8], and the experimental data provide possibilities to constrain the $N\Lambda$ and $\Lambda\Lambda$ interactions. New research plans [9] open good opportunities to investigate the low-lying energy spectra for both single- and double-Λ hypernuclei.

Among various theoretical approaches, the shell model was used to describe the low-lying energy spectra of light (with a *p*-shell nuclear core) single- and double-Λ hypernuclei [10–13]. Within a few-body model, the cluster structure of single- and double-Λ hypernuclei was investigated, and the energy spectra, electromagnetic transition rates, and hypernuclear matter distributions were reproduced successfully [14–17]. Also for light hypernuclei, an *ab initio* calculation based on realistic nucleonic and hyperonic interactions was extended to ${}^{13}_{\Lambda}$C [18]. For *sd*-shell Λ hypernuclei, the antisymmetrized molecular dynamics (AMD) allows very detailed investigations [19–22] and was recently also extended to study the cluster structure of ${}^{10}_{\Lambda}$Be and ${}^{11}_{\Lambda}$Be [23].

Compared with the theoretical models mentioned above, the hypernuclear energy density functional theories including Skyrme–Hartree–Fock (SHF) and relativistic mean-field (RMF) models are suitable to investigate not only light, but also medium and heavy hypernuclei. The SHF model was first extended to Λ hypernuclei by using Skyrme-type $N\Lambda$ interactions in Ref. [24]. A generalized SHF model employing effective $N\Lambda$ interactions derived from the Nijmegen soft-core potentials [25–28] or Skyrme-type $N\Lambda$ interactions [29] was used with a spherical mean-field configuration to study the properties of single- and double-Λ hypernuclei, and later quadrupole constraints and pairing interactions were included into this model [30–32]. The shape evolution in isotope chains due to the addition of one Λ was first studied in the hypernuclear RMF model [33], and then the impurity effect of a Λ in various *p*- and *sd*-shell hypernuclei was investigated in a triaxial SHF model [34]. The (super)deformation of hypernuclei was recently investigated within a multidimensionally constrained RMF model [35,36] and AMD [37].

Considering the importance of low-lying energy spectra and electric multipole transition strengths in the study of hypernuclei, it is worthwhile to mention several kinds of beyond-mean-field calculations for Λ hypernuclei in recent years. Based on the hypernuclear RMF model, the particle-rotor model and the five-dimensional collective Hamiltonian (5DCH) were extended to investigate the low-lying states of hypernuclei and the impurity effect of the Λ [38–42], and then the RMF model equipped with angular-momentum projection (AMP) techniques and the generator coordinate method (GCM) was used to obtain the energy spectrum and electric-quadrupole transition strengths of ${}^{21}_{\Lambda}$Ne [43]. For the deformed hypernuclear SHF model, AMP and particle number projection (PNP) techniques were used to restore the rotational symmetry and particle number [44], but the mixing of configurations with different shapes was neglected due to the absence of the GCM.

In this paper, aiming at constructing a unified model to investigate low-lying energy spectra of both single- and double-Λ hypernuclei, a beyond-mean-field calculation (including AMP techniques and GCM) based on the hypernuclear SHF model is derived and implemented to ${}^{13}_{\Lambda}$C, ${}^{14}_{\Lambda\Lambda}$C, ${}^{21}_{\Lambda}$Ne, and ${}^{22}_{\Lambda\Lambda}$Ne. This paper is organized as follows: In Sec. II the formalism of the beyond-mean-field calculation is introduced,

*xrzhou@phy.ecnu.edu.cn
†lxguo@xidian.edu.cn

Sec. III presents the results and discussions, and in Sec. IV we summarize the work.

II. FORMALISM

The hypernuclear states are described by a superposition of angular-momentum-projected mean-field wave functions

$$|\Psi_\alpha^{JM}\rangle = \sum_\beta F_\alpha^J(\beta)\hat{P}_{MK}^J|\Phi^{(N\Lambda)}(\beta)\rangle, \tag{1}$$

where $F_\alpha^J(\beta)$ is the weight function and $\hat{P}_{MK}^J$ is an AMP operator with $K = K_c + K_Y$ being the projection of angular momentum J^π on the intrinsic z axis, and K_c and K_Y are the components of the nuclear core and of the hyperons, respectively. The assumption of time-reversal symmetry for the axially deformed nuclear core leads to $K_c = 0$ and $K_Y = \pm 1/2, 0$ for single- or double-Λ hypernuclei, respectively.

The hypernuclear mean-field wave function from the hypernuclear SHF calculation with a quadrupole constraint is given by

$$|\Phi^{(N\Lambda)}(\beta)\rangle = |\Phi^N(\beta)\rangle \otimes |\Phi^\Lambda\rangle, \tag{2}$$

where $|\Phi^N(\beta)\rangle$ and $|\Phi^\Lambda\rangle$ are intrinsic wave functions of the nuclear core with quadrupole deformation β and of the hyperons, respectively. The deformation parameter β of the nuclear core is proportional to the quadrupole moment as

$$\beta = \frac{4\pi}{3A_cR_0^2}\langle\Phi^N(\beta)|r^2Y_{20}|\Phi^N(\beta)\rangle, \tag{3}$$

where A_c is the mass number of the core nucleus and $R_0 = 1.2A_c^{1/3}$ fm, and it is slightly different from the definition in Ref. [43], but will not influence the current calculation.

Each weight $F_\alpha^J(\beta)$ in Eq. (1) is determined by the Hill–Wheeler–Griffin (HWG) equation [45]

$$\sum_{\beta'}\left[H'^J_{KK}(\beta,\beta') - E_\alpha^J N_{KK}^J(\beta,\beta')\right]F_\alpha^J(\beta') = 0, \tag{4}$$

where the Hamiltonian and norm elements are given by

$$H'^J_{KK'}(\beta,\beta') = \langle\Phi^{(N\Lambda)}(\beta')|\hat{H}'\hat{P}_{KK'}^J|\Phi^{(N\Lambda)}(\beta)\rangle, \tag{5}$$

$$N_{KK'}^J(\beta,\beta') = \langle\Phi^{(N\Lambda)}(\beta')|\hat{P}_{KK'}^J|\Phi^{(N\Lambda)}(\beta)\rangle. \tag{6}$$

The relation between the Hamiltonians $\hat{H}'$ and $\hat{H}$ is

$$\hat{H}' = \hat{H} - \lambda_p(\hat{N}_p - Z) - \lambda_n(\hat{N}_n - N), \tag{7}$$

where the last two terms on the right-hand side account for the fact that the projected wave function does not provide the correct number of particles on average [46–48].

When the weight function $F_\alpha^J(\beta)$ is determined, the neutron or proton root-mean-square (rms) radius is defined as

$$R_{\rm rms}^{J\alpha} = \sqrt{\sum_{\beta\beta'} F_\alpha^{J*}(\beta')F_\alpha^J(\beta)\langle\Phi^{(N\Lambda)}(\beta')|r^2\hat{P}_{KK}^J|\Phi^{(N\Lambda)}(\beta)\rangle}, \tag{8}$$

and the reduced $E2$ transition rate is derived as

$$B(E2, J\alpha \to J'\alpha') = \frac{1}{2J+1}|\langle\alpha'; J'||\hat{Q}_2||\alpha; J\rangle|^2, \tag{9}$$

where

$$\langle\alpha'; J'||\hat{Q}_2||\alpha; J\rangle = \sqrt{2J'+1}\sum_{M\mu\beta\beta'} F_{\alpha'}^{J'*}(\beta')F_\alpha^J(\beta)C_{JM2\mu}^{J'K'} \times \langle\Phi^{(N\Lambda)}(\beta')|\hat{Q}_{2\mu}\hat{P}_{MK}^J|\Phi^{(N\Lambda)}(\beta)\rangle, \tag{10}$$

in which $\hat{Q}_{2\mu} = r^2Y_{2\mu}(\varphi,\theta)$ is the electric-quadrupole transition operator [49] and $C_{JM2\mu}^{J'K'}$ denotes the Clebsh–Gordon coefficients.

Obtained from the hypernuclear SHF calculation with density-dependent delta interaction (DDDI) [50], the BCS wave function for the nuclear core, $|\Phi^N(\beta)\rangle$ in Eq. (2), is written as

$$|\Phi^N(\beta)\rangle = \prod_{k>0}(u_k + v_k a_k^+ a_{\bar{k}}^+)|{\rm HF}\rangle, \tag{11}$$

and the wave function for the hyperons is

$$|\Phi^\Lambda\rangle = \varphi_s(\Lambda) \tag{12}$$

for single-Λ hypernuclei and an antisymmetrized one,

$$|\Phi^\Lambda\rangle = \frac{1}{\sqrt{2}}[\varphi_s(\Lambda_1)\varphi_{\bar{s}}(\Lambda_2) - \varphi_s(\Lambda_2)\varphi_{\bar{s}}(\Lambda_1)], \tag{13}$$

for double-Λ hypernuclei, where φ_s and $\varphi_{\bar{s}}$ are time-reversal partners of the s_Λ orbit. It has been shown in Refs. [14] and [42] that the positive-parity J_α^+ hypernuclear excited states are dominated by the $\Lambda_s \otimes I_\alpha^+$ configurations and thus the coupling to Λ_p states is neglected in this current work.

Since the projected states do not form an orthogonal basis, $F_\alpha^J(\beta)$ are nonorthogonal functions [42], and orthogonal collective wave functions are constructed as

$$g_\alpha^J(\beta) = \sum_{\beta'}[\mathcal{R}^{\frac{1}{2}}]^J(\beta,\beta')F_\alpha^J(\beta'), \tag{14}$$

which are weights of the natural states in the collective subspace [45], and where

$$[\mathcal{R}^{\frac{1}{2}}]^J(\beta,\beta') = \sum_k \sqrt{n_k}\, w_k(\beta)w_k^*(\beta'), \tag{15}$$

with the eigenfunctions w_k and eigenvalues n_k of the norm operator, Eq. (6), in the projected space. The average deformation

$$\bar{\beta} = \sum_\beta |g_\alpha^J(\beta)|^2\beta \tag{16}$$

reflects the shape of the dominant configuration in the ground or excited state and indicates the band structure [51].

In Refs. [34,52,53] the SGII Skyrme force [54] was employed to investigate carbon and neon isotopes and the corresponding Λ hypernuclei, and the same Skyrme force is used in this current calculation, while the spin-orbit term is reduced to 70% for carbon (hyper)nuclei to give the right energy of the first-excited state. The strength of the density-dependent pairing interaction is $V = -410$ MeV fm^3 for both protons and neutrons, and a smooth pairing energy cutoff of 5 MeV around the Fermi level is used [34,55]. For the $N\Lambda$ and $\Lambda\Lambda$ parts, the density-dependent effective interactions derived

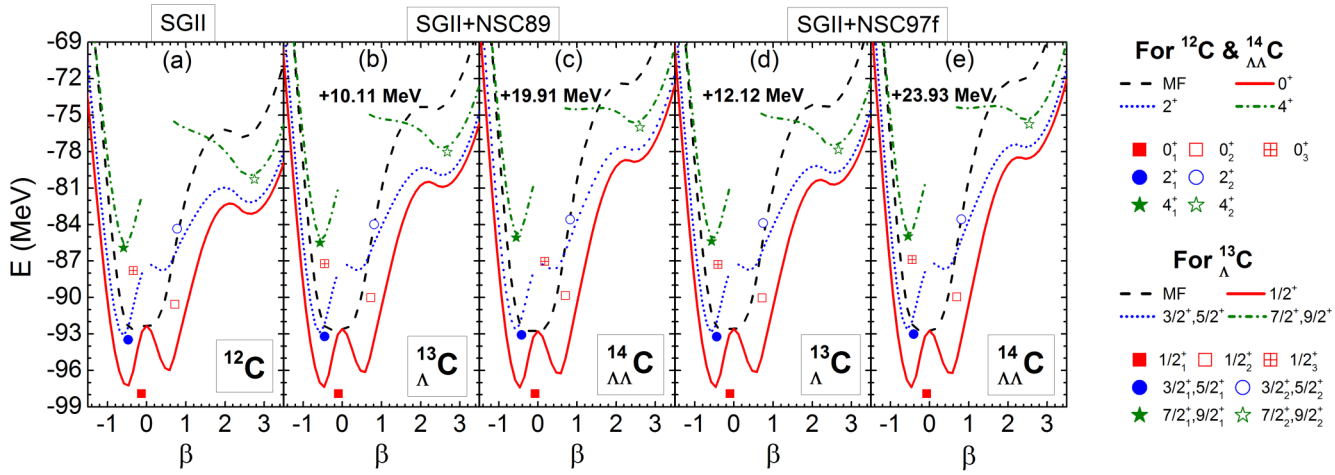

FIG. 1. Potential-energy surfaces as functions of deformation parameter β from mean-field calculation and AMP for (a) ^{12}C and (b), (c) $^{13}_{\Lambda}$C and $^{14}_{\Lambda\Lambda}$C using the NSC89 or (d), (e) NSC97f force. The symbols represent the GCM states with given J^{π}, located at the average deformation $\bar{\beta}$ of Eq. (16). Offsets are used for hypernuclei according to the (double-)Λ binding energies to keep the ground states of all the (hyper)nuclei at the same level. The spin doublets are represented by one single curve or symbol due to their negligible splitting.

from the Nijmegen soft-core interactions NSC89 and NSC97f [28] are employed and the hypernuclear spin-orbit forces are excluded according to Refs. [28,34].

III. RESULTS

Using the beyond-mean-field SHF model introduced in the previous section, ^{12}C, ^{20}Ne, and the corresponding (double-)Λ hypernuclei, i.e., $^{13}_{\Lambda}$C, $^{14}_{\Lambda\Lambda}$C, $^{21}_{\Lambda}$Ne, and $^{22}_{\Lambda\Lambda}$Ne, are investigated. Their energy spectra, $E2$ transition rates, and the shrinkage effects of Λs are discussed in this section.

A. Study of ^{12}C, $^{13}_{\Lambda}$C, and $^{14}_{\Lambda\Lambda}$C

Figure 1(a) shows the potential-energy surfaces (PESs) with given J^{π} as a function of the deformation parameter β from mean-field calculation and AMP for the core nucleus ^{12}C. The most obvious effect is the energy gained by AMP, which changes the mean-field PES with a flat curve and near spherical shape into the $J^{\pi} = 0^{+}$ one with two pronounced minima at oblate and prolate shapes, respectively. A similar phenomenon happens for the beyond-RMF calculation in Ref. [42], but the barrier between the two minima is much smaller than the one in our current calculation. The energies from the GCM calculation located at the average shape $\bar{\beta}$ are also shown in the same panel. The energy of the first 2^{+} state is 4.44 MeV, which reproduces precisely the observed one [56] with the reduced SGII force introduced at the end of the last section. The second 0^{+} state locates at 7.34 MeV, and it seems very close to the observed Hoyle state (7.65 MeV [57–59]), but in fact it is difficult for the current model to reproduce the Hoyle state due to its dilute cluster structure [60–62].

Figures 1(b)–1(e) shows the PES patterns and energy levels from the GCM calculation for $^{13}_{\Lambda}$C and $^{14}_{\Lambda\Lambda}$C, using the NSC89 and NSC97f forces. The addition of a single- or double-Λ makes the PES slightly stiffer for both mean-field or AMP calculations, as an impurity effect of the Λs, which occupy the $s_{1/2}$ orbit and have a stronger attractive interaction with a spherical nuclear core than with a deformed one. In Figs. 1(b) and 1(d), the $(3^{+}/2,\ 5^{+}/2)$ and the $(7^{+}/2,\ 9^{+}/2)$ states are represented by the same symbols, respectively, because the spin splitting of these states is almost zero due to the absence of a $N\Lambda$ spin-orbit term in the Hamiltonian.

In Ref. [28] four parameter sets for different density-dependent Nijmegen soft-core interactions were used to investigate the properties of single- and double-Λ hypernuclei, and it was shown that the NSC89 and NSC97f forces yield the better overall reproduction of hypernuclear binding energies. In our current beyond-mean-field calculation, using the ground-state energies obtained by the GCM, the single- and double-Λ removal energies of $^{13}_{\Lambda}$C and $^{14}_{\Lambda\Lambda}$C are 10.1 and 19.9 MeV for the NSC89 force, and 12.1 and 23.9 MeV for the NSC97f force, respectively, compared with the experimental value of 11.7 MeV for $^{13}_{\Lambda}$C [63].

The average deformations of the ground states in ^{12}C, $^{13}_{\Lambda}$C, and $^{14}_{\Lambda\Lambda}$C using the NSC97f force are $\bar{\beta} = -0.130, -0.101$, and -0.075, respectively, as shown in Figs. 1(a), 1(d), and 1(e), which indicates that the addition of the Λs drives the average shape towards the spherical region, and the same phenomenon also happens for the NSC89 force. This trend is caused by the fact that the Λ located in an s orbit favors a spherical nuclear core and slightly prefers a prolate nuclear core to an oblate one, as explained in more detail in Ref. [34].

This influence of Λs on the core nucleus is shown more clearly in Fig. 2, which displays the collective wave functions g^{J}_{α} of ^{12}C in Fig. 2(a) and Δ_J of $^{14}_{\Lambda\Lambda}$C with $J = 0^{+}_{1}, 2^{+}_{1}$, and 4^{+}_{1} in Figs. 2(b), 2(c), and 2(d), respectively. The quantity

$$\Delta_J(\beta) = \left|g^{J}_{\alpha=1}(\beta)\right|_H - \left|g^{J}_{\alpha=1}(\beta)\right|_c \qquad (17)$$

is introduced to describe the change of the absolute value of $g^{J}_{\alpha}(\beta)$ when two Λs are added. The subscripts H and c denote $g^{J}_{\alpha}(\beta)$ for a hypernucleus and a core nucleus, respectively. We can see that, due to the addition of Λs, the absolute value of g^{J}_{α} of the 0^{+}_{1} state in $^{14}_{\Lambda\Lambda}$C decreases in the $\beta < -0.5$ domain and increases in the $-0.5 < \beta < 1.2$ domain compared with the

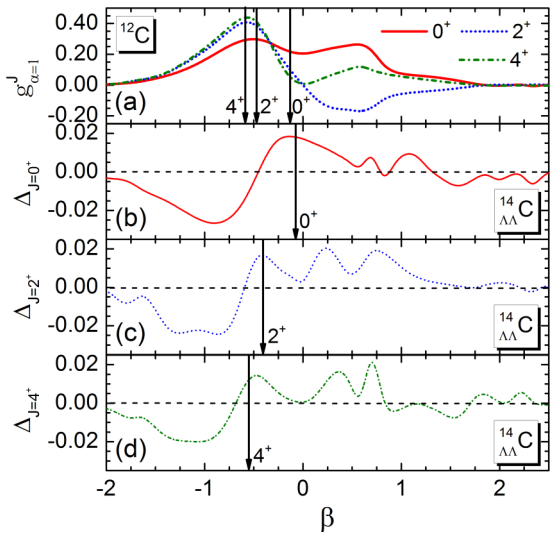

FIG. 2. Collective wave functions $g^J_\alpha(\beta)$ for the GCM states of the ground band with $J^\pi = 0^+,2^+,4^+$ (a) of ^{12}C, and the change Δ_J, Eq. (17), due to the addition of double-Λ for (b)–(d) $^{14}_{\Lambda\Lambda}$C using the NSC97f force. The arrows indicate $\bar{\beta}$ for each state of ^{12}C and $^{14}_{\Lambda\Lambda}$C.

one in ^{12}C. Figure 2 also indicates the position of the average deformation $\bar{\beta}$ of each state by arrows, and the reduction of $\bar{\beta}$ is seen clearly. Similar phenomena happen in the case of the 2^+_1 and 4^+_1 states. An equivalent behavior of g^J_α also exists in $^{13}_{\Lambda}$C but is not so obvious as in $^{14}_{\Lambda\Lambda}$C.

The ground-band energy levels and electric-quadrupole transition strengths are shown in Fig. 3 for ^{12}C, $^{13}_{\Lambda}$C, and $^{14}_{\Lambda\Lambda}$C. The addition of Λs enlarges the excitation energies, because it reduces both the radius and deformation of the system, which leads to a reduced moment of inertia and increases the distance of the rotational levels [64]. The reduced radius and shape deformation also lead to the reduction of $E2$ transition rates shown in Fig. 3, which will be discussed in detail below.

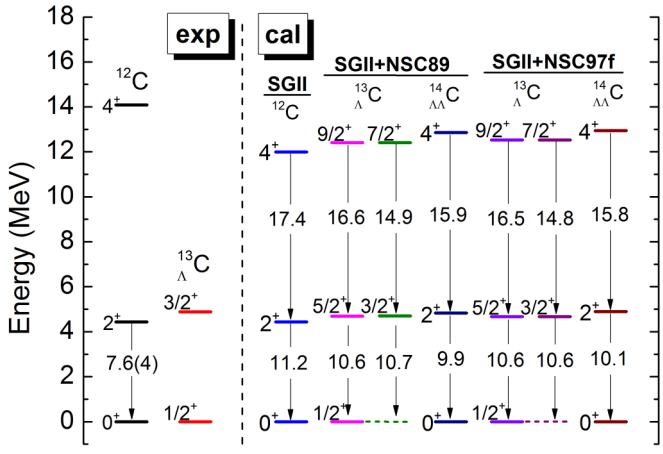

FIG. 3. Energy spectra of ^{12}C, $^{13}_{\Lambda}$C, and $^{14}_{\Lambda\Lambda}$C, using the $N\Lambda$ interaction parameters NSC89 and NSC97f. Electric-quadrupole transition strengths $B(E2)$ are shown in e^2 fm^4 along the arrows. The experimental data are taken from Refs. [56–59] for ^{12}C and Ref. [6] for $^{13}_{\Lambda}$C.

TABLE I. Core transition rates $cB(E2)$ and relative change Δ, Eq. (19), in $^{13}_{\Lambda}$C using the NSC89 and NSC97f interaction, respectively. Beyond-RMF results using the PC-F1 force are taken from Ref. [42]. The unit of $B(E2)$ and $cB(E2)$ is e^2 fm^4.

$J^\pi_i \to J^\pi_f$	NSC89			NSC97f		PC-F1
	$B(E2)$	$cB(E2)$	Δ(%)	$cB(E2)$	Δ(%)	Δ(%)
$3/2^+_1 \to 1/2^+_1$	10.66	10.66	−5.00	10.56	−5.93	−14.17
$5/2^+_1 \to 1/2^+_1$	10.63	10.63	−5.26	10.56	−5.89	−14.17
$7/2^+_1 \to 3/2^+_1$	14.90	16.56	−4.60	16.49	−5.00	−21.36
$7/2^+_1 \to 5/2^+_1$	1.66	16.58	−4.48	16.49	−5.00	−21.35
$9/2^+_1 \to 5/2^+_1$	16.57	16.57	−4.51	16.49	−5.00	−21.36

For a comprehensive understanding of the shrinkage effect reflected by the $B(E2)$ values, it is worthwhile to make a comparison of results of the current calculation and the beyond-RMF calculation in Ref. [42]. As in that reference, the quantity

$$cB(E2, I_i \to I_f) = \frac{1}{(2I_i+1)(2J_f+1)} \begin{Bmatrix} I_f & J_f & j_i \\ J_i & I_i & 2 \end{Bmatrix}^{-2} \times B(E2, J_i \to J_f) \tag{18}$$

is introduced to remove the trivial factor due to the angular-momentum coupling for the $s_{1/2}$ state of the Λ particle, where c emphasizes the "core transition." In Table I, the $cB(E2)$ values of $^{13}_{\Lambda}$C and the relative shrinkage [42]

$$\Delta \equiv \frac{cB(E2) - B(E2;^{12}\mathrm{C})}{B(E2;^{12}\mathrm{C})} \tag{19}$$

are given and compared with the results of Ref. [42]. We can see that $B(E2,2^+_1 \to 0^+_1)$ is reduced by 5%–6% in this current work, whereas Ref. [42] reports a stronger reduction of about 14%. One reason for the difference between the two models is that the beyond-RMF model gives a more shallow projected energy curve near the two minima than the beyond-SHF model does. In Fig. 1(a), it is shown that the barrier between the two energy minima with $J^\pi = 0^+$ is about 4 MeV, while it is just 1 MeV or less in Fig. 2 of Ref. [42]. As shown in Fig. 2 of this current paper, the addition of Λs makes the configuration with small β more dominant, which causes the reduction of $B(E2)$. But the large barrier between the two energy minima hinders such trend in $^{13}_{\Lambda}$C, which makes the reduction of $B(E2)$ in this current work weaker than in Ref. [42]. Actually, the shrinkage of $^{13}_{\Lambda}$C is commonly very strong in RMF calculations. In Ref. [35], the addition of one Λ turns the oblate ^{12}C into a spherical one and reduces the proton radius from 2.57 to 2.50 fm.

To show in full detail where the reduction of the $B(E2)$ values in $^{13}_{\Lambda}$C and $^{14}_{\Lambda\Lambda}$C comes from, we introduce as in Ref. [14] the ratio

$$\Gamma_B = \frac{cB(E2,2^+_1 \to 0^+_1;^{13}_{\Lambda}\mathrm{C})}{B(E2,2^+_1 \to 0^+_1;^{12}\mathrm{C})} = 1 - \Delta. \tag{20}$$

Provided the simple assumption that the $B(E2)$ value is proportional to the square of the intrinsic quadrupole moment

TABLE II. Root-mean-square charge radii r_c in unit of fm, and the ratios Γ_r, Γ_β, Γ_B according to Eq. (23) of ^{12}C, $^{13}_{\Lambda}$C, and $^{14}_{\Lambda\Lambda}$C using different $N\Lambda$ interactions.

	^{12}C	$^{13}_{\Lambda}$C				$^{14}_{\Lambda\Lambda}$C			
	r_c	r_c	Γ_r	Γ_β	Γ_B	r_c	Γ_r	Γ_β	Γ_B
NSC89	2.58	2.56	0.964	0.985	0.950	2.54	0.933	0.950	0.886
NSC97f		2.56	0.962	0.978	0.941	2.54	0.936	0.957	0.895

Q_0 [45],

$$B(E2, I+2 \to I) = \frac{5}{16\pi} Q^2_{I+2\to I},$$
$$Q^2_{I+2\to I} = Q_0^2 \left| C^{I+22I}_{K\ 0K} \right|^2, \tag{21}$$

and using the approximation to first order in β for moderate deformation [32,65],

$$Q_0 \approx Ze\sqrt{\frac{16\pi}{5}}\frac{3}{4\pi}R_0^2\beta \approx Ze\sqrt{\frac{5}{\pi}}\langle r^2\rangle\beta, \tag{22}$$

Γ_B is expressed approximately as the product of two factors

$$\Gamma_B \approx \frac{Q_{c0}^2}{Q_0^2} = \Gamma_r\Gamma_\beta, \tag{23}$$

in which $\langle r^2\rangle^{1/2}$ is the rms charge radius of ^{12}C, while Q_{c0} and $\langle r_c^2\rangle^{1/2}$ are the same quantities of the nuclear cores in $^{13}_{\Lambda}$C or $^{14}_{\Lambda\Lambda}$C. The ratio $\Gamma_r \equiv \langle r_c^2\rangle^2/\langle r^2\rangle^2$ indicates the reduction of the size of the nuclear core, whereas $\Gamma_\beta \equiv \beta_c^2/\beta^2$ measures the effect caused by the change of β.

The GCM calculation in this current paper shows, however, that there are no well-defined shapes for the ground band of ^{12}C, $^{13}_{\Lambda}$C, and $^{14}_{\Lambda\Lambda}$C. For example, while the ground state of ^{12}C is a "spread" one, the 2^+_1 state is oblately deformed, as shown in Fig. 2. So it is difficult to derive Γ_β from the shape parameters β and β_c. However, according to Eq. (23), it can be estimated by $\Gamma_\beta \approx \Gamma_B/\Gamma_r$, since in our calculation Γ_B and Γ_r are explicitly derived by $E2$ transition rates and rms charge radii, respectively.

In Table II, the rms charge radii r_c and the ratios Γ_r, Γ_B, Γ_β of the different (hyper)nuclei are listed. One can see that the addition of Λs always leads to a shrinkage of the charge radius and that Γ_r is smaller than Γ_β in all cases. This means that the reduction of the $E2$ transition strengths in the nuclear core is mainly due to the shrinkage of the charge radii, but also the reduced shape deformation plays a non-negligible role.

In our calculation, the spectroscopic quadrupole moment $Q_{2\to 2}$ of the 2^+_1 state, Eq. (10) with $\alpha = \alpha' = 1$ and $J = J' = 2^+$, is calculated for ^{12}C and its value is $Q(b) = +0.074$ compared with the experimental one $+0.06(3)$ [66]. Also for ^{20}Ne, which will be discussed in the next section, the calculated and experimental $Q(b)$ values are -0.205 and $-0.23(3)$ [66], respectively. According to Eq. (21), these differences between calculated and experimental Q values are closely related to the differences of the $B(E2)$ values shown in Figs. 3 and 5.

B. Study of ^{20}Ne, $^{21}_{\Lambda}$Ne, and $^{22}_{\Lambda\Lambda}$Ne

The hypernucleus $^{21}_{\Lambda}$Ne has been studied in various theoretical models [20,42,43,67] and is thus suitable for a comparison of the different approaches. In this section, we give a uniform description of ^{20}Ne, $^{21}_{\Lambda}$Ne, and $^{22}_{\Lambda\Lambda}$Ne in our beyond-SHF model and investigate in detail the reduction of $B(E2)$.

For ^{20}Ne, Fig. 4(a) shows the energy curves from mean-field calculations and AMP, and the GCM levels are indicated by symbols at the average deformations $\bar\beta$. The most obvious difference to the case of $^{13}_{\Lambda}$C is the very strong deformation of $\bar\beta \approx 0.5$ already at the mean-field level and persisting in all excited states. The 0^+ curve in our current work is qualitatively the same as the one obtained in the beyond-RMF calculation [42], with similar deformation, but with a larger barrier between the two energy minima. Figures 4(b)–4(e) give the energy curves of $^{21}_{\Lambda}$Ne and $^{22}_{\Lambda\Lambda}$Ne in an offset manner, using the NSC89 and NSC97f forces. The single- and double-Λ binding energies are 13.6 and 26.8 MeV for the NSC89 force, while 15.9 and 31.4 MeV for the NSC97f force, respectively. The average deformation $\bar\beta$ reduces from 0.514 to 0.483 and 0.433 in ^{20}Ne, $^{21}_{\Lambda}$Ne, and $^{22}_{\Lambda\Lambda}$Ne, respectively, for the NSC97f force. As in the case of $^{13}_{\Lambda}$C, the absence of a hypernuclear

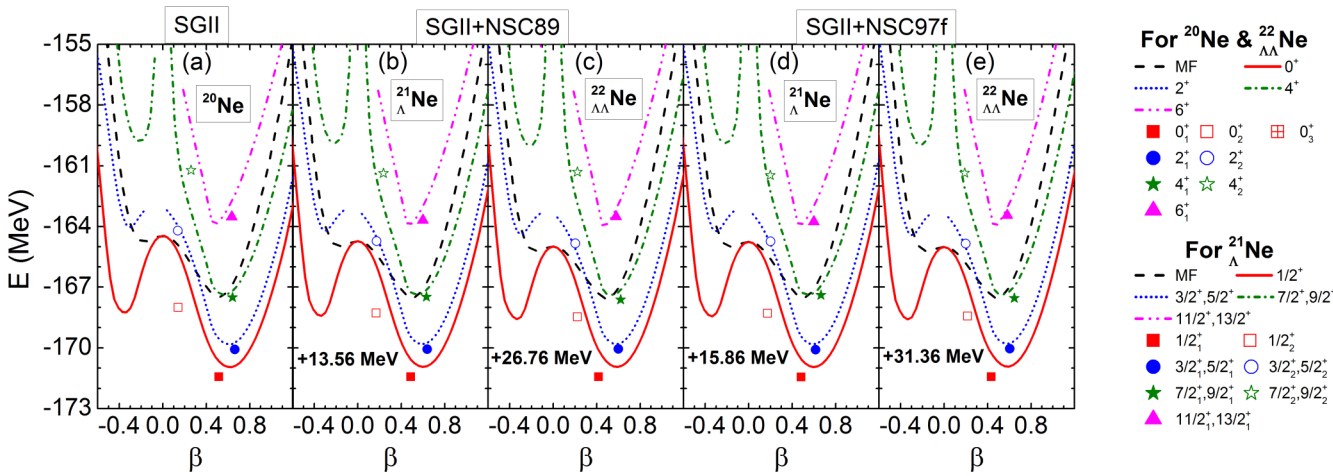

FIG. 4. Same as in Fig. 1, but for ^{20}Ne, $^{21}_{\Lambda}$Ne, and $^{22}_{\Lambda\Lambda}$Ne.

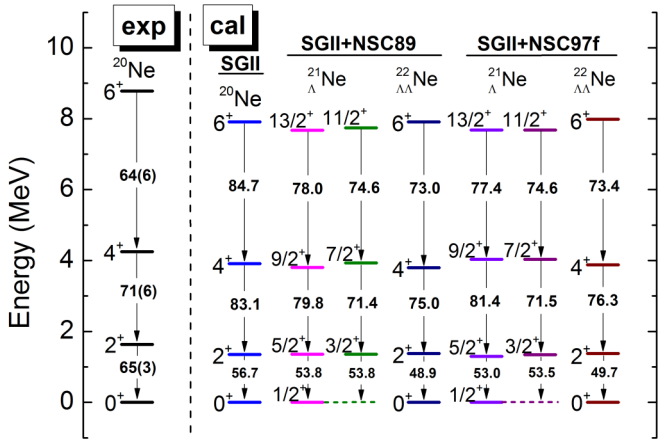

FIG. 5. Same as in Fig. 3, but for ^{20}Ne, $^{21}_{\Lambda}$Ne, and $^{22}_{\Lambda\Lambda}$Ne. The experimental data are taken from Ref. [56].

spin-orbit term makes the spin splitting very small, and it is not shown in the figure.

In Fig. 5, we display the ground bands of ^{20}Ne, $^{21}_{\Lambda}$Ne, and $^{22}_{\Lambda\Lambda}$Ne, and the $B(E2)$ values between the rotational levels. The calculated 2^+_1 state of ^{20}Ne is at 1.35 MeV compared with the observed one at 1.63 MeV, and the $B(E2)$ value also coincides satisfactorily with the observed one. This $B(E2)$ value is reduced by about 5%–7% in $^{21}_{\Lambda}$Ne and 12%–14% in $^{22}_{\Lambda\Lambda}$Ne.

To make a comprehensive comparison with other models, we list in Table III the reduction of $cB(E2)$ in $^{21}_{\Lambda}$Ne in this current calculation and those in different kinds of models including the beyond-RMF model, clustering model [67], and AMD [20]. It is shown that the reduction of $cB(E2)$ in our calculation is stronger than that in the beyond-RMF model with PC-F1 parameters, but weaker than that with PC-PK1 parameters. The clustering model and AMD give much larger reductions than both our calculation and the beyond-RMF calculation [42].

But recently a more self-consistent beyond-RMF calculation using AMP and GCM techniques obtained a reduction of $cB(E2,2^+_1 \to 0^+_1)$ in $^{21}_{\Lambda}$Ne of more than 12% [43]. In that reference the $J^\pi = 1/2^+$ projected energy curve has two energy minima with prolate and oblate shapes, respectively, and that pattern is similar to the one in our current calculation

TABLE III. Reduction Δ, Eq. (19), of the core nuclear transition $cB(E2)$ in $^{21}_{\Lambda}$Ne. For comparison, the results using beyond-RMF model (PC-F1 and PC-PK1) [42], AMD [20], and cluster model [67] are given.

$J^\pi_i \to J^\pi_f$	NSC89 Δ(%)	NSC97f Δ(%)	PC-F1 Δ(%)	PC-PK1 Δ(%)	AMD Δ(%)	Cluster Δ(%)
$3/2^+_1 \to 1/2^+_1$	−5.08	−5.64	−3.19	−7.16	−11.8	−23.9
$5/2^+_1 \to 1/2^+_1$	−5.08	−6.51	−3.19	−7.16	−11.5	
$7/2^+_1 \to 3/2^+_1$	−4.55	−4.40	−3.95	−4.80	−17.8	−22.6
$7/2^+_1 \to 5/2^+_1$	−4.55	−2.00	−3.95	−4.80		
$9/2^+_1 \to 5/2^+_1$	−3.98	−2.00	−3.95	−4.81	−13.0	

TABLE IV. Same as Table II, but for ^{20}Ne, $^{21}_{\Lambda}$Ne, and $^{22}_{\Lambda\Lambda}$Ne.

	^{20}Ne	$^{21}_{\Lambda}$Ne				$^{22}_{\Lambda\Lambda}$Ne			
	r	r_c	Γ_r	Γ_β	Γ_B	r_c	Γ_r	Γ_β	Γ_B
NSC89	2.92	2.91	0.977	0.971	0.949	2.88	0.948	0.910	0.863
NSC97f		2.90	0.975	0.967	0.944	2.89	0.952	0.922	0.877

(Fig. 4), but with a much smaller barrier between the two energy minima. The barrier is nearly 4 MeV in our current calculation, but less than 1 MeV in Ref. [43]. As discussed in the previous section, this softness of the PES is (at least one of) the reason(s) why the beyond-RMF calculation [43] obtains a larger reduction of $cB(E2)$ in $^{21}_{\Lambda}$Ne than our current calculation does. Furthermore, in Ref. [42], the PES with PC-PK1 parameters is slightly softer than that with PC-F1 parameters, and the reduction of $B(E2)$ values corresponding to PC-PK1 parameters is indeed larger than the one from PC-F1 parameters (see Table III), in line with the argument above.

In analogy to the last section, we investigate the major cause for the reduction of $cB(E2)$ in $^{21}_{\Lambda}$Ne and $^{22}_{\Lambda\Lambda}$Ne, through the comparison of Γ_r and Γ_β, which indicate the change of charge radius and shape deformation, respectively. Table IV shows the values of Γ_r and Γ_β in $^{21}_{\Lambda}$Ne and $^{22}_{\Lambda\Lambda}$Ne using the NSC89 force and NSC97f force, respectively. Γ_β is always smaller than Γ_r, which indicates that in this case the decrease of shape deformation plays a more important role for the reduction of the $B(E2)$ transition.

This result is opposite to the case of $^{13}_{\Lambda}$C and $^{14}_{\Lambda\Lambda}$C discussed in the previous section, which might be explained by two possible reasons. First, the deformation of ^{20}Ne is much larger than that of ^{12}C, and therefore the added Λs might cause a bigger effect. Second, the different compactness of nucleons in ^{12}C and ^{20}Ne, i.e., the average density of nuclear matter is larger in ^{20}Ne than that in ^{12}C. In Fig. 6, we give the nuclear density distribution of the ground state of ^{12}C and ^{20}Ne. It is shown that the density of nuclear matter in ^{20}Ne is larger than the one in ^{12}C and reaches more than 0.16 fm^{-3} in the center of ^{20}Ne. The saturation of nuclear density in ^{20}Ne hinders the

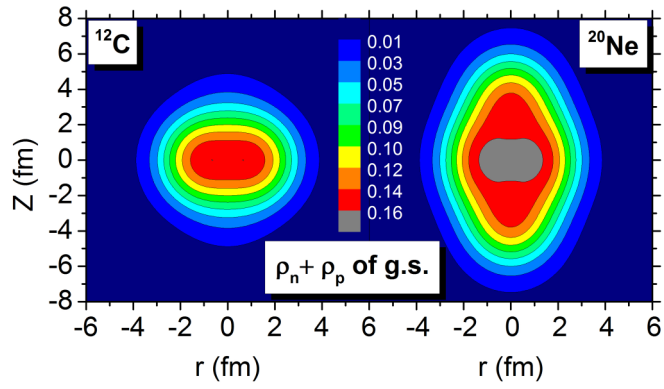

FIG. 6. Nuclear density distribution of the ground states for ^{12}C and ^{20}Ne. An identical color bar is used for both nuclei.

Λs from shrinking the radius, which is not the case for ^{12}C with a more dilute density.

IV. CONCLUSIONS

Based on a hypernuclear SHF model with realistic $N\Lambda$ interactions, AMP techniques, and GCM, we investigated the energy spectra and the reduced $E2$ transition rates of the cores in $^{13}_{\Lambda}$C, $^{14}_{\Lambda\Lambda}$C, $^{21}_{\Lambda}$Ne, and $^{22}_{\Lambda\Lambda}$Ne, and compared them to those of ^{12}C and ^{20}Ne, respectively. The projected energy curves with different angular momenta as functions of β were obtained and we found that the addition of Λs makes the PES slightly stiffer.

As an impurity effect, the Λs lead to reduced $cB(E2)$ values. Through the comparison with the results of other models, especially the beyond-RMF models [42,43], we found that the reduction of $cB(E2)$ in our calculation for $^{13}_{\Lambda}$C and $^{21}_{\Lambda}$Ne is smaller than that in the beyond-RMF model, and the reason is that the projected PES derived from the beyond-RMF model is softer than the one from the current calculation. Different advanced theoretical approaches thus predict quantitatively different results for the deformation properties, and this is an important problem to address in future work.

A further analysis was made to investigate the reduction of the charge radius and shape deformation β of the nuclear cores. We found that the reduction of the $E2$ transition strengths in $^{13}_{\Lambda}$C and $^{14}_{\Lambda\Lambda}$C is mainly due to the charge-radius shrinkage of the nuclear core, while the reduced shape deformation also plays an important role. On the contrary, in the much stronger deformed $^{21}_{\Lambda}$Ne and $^{22}_{\Lambda\Lambda}$Ne the reduction of shape deformation is the dominant reason for the reduced $cB(E2)$.

ACKNOWLEDGMENTS

The authors thank X. Y. Wu, J. M. Yao, and E. Hiyama for helpful discussions. This work was supported by the National Natural Science Foundation of China (Grants No. 11547044 and No. 11275160) and supported by the Fundamental Research Funds for the Central Universities (Grants No. JB160510 and No. XJS15060).

[1] O. Hashimoto and H. Tamura, Prog. Part. Nucl. Phys. **57**, 564 (2006).
[2] E. Botta, T. Bressani, and G. Garbarino, Eur. Phys. J. A **48**, 41 (2012).
[3] A. Gal and E. V. Hungerford, Rev. Mod. Phys. **88**, 035004 (2016).
[4] K. Tanida *et al.*, Phys. Rev. Lett. **86**, 1982 (2001).
[5] S. Ajimura *et al.*, Phys. Rev. Lett. **86**, 4255 (2001).
[6] H. Kohri *et al.*, Phys. Rev. C **65**, 034607 (2002).
[7] S. Aoki *et al.*, Nucl. Phys. A **828**, 191 (2009).
[8] K. Nakazawa *et al.*, Nucl. Phys. A **835**, 207 (2010).
[9] H. Tamura, Prog. Theor. Exp. Phys. 02B012 (2012).
[10] A. Gal, J. M. Soper, and R. H. Dalitz, Ann. Phys. (NY) **63**, 53 (1971).
[11] A. Gal, J. M. Soper, and R. H. Dalitz, Ann. Phys. (NY) **72**, 455 (1972).
[12] A. Gal, Nucl. Phys. A **754**, 91c (2005).
[13] A. Gal and D. J. Millener, Phys. Lett. B **701**, 342 (2011).
[14] E. Hiyama, M. Kamimura, T. Motoba, T. Yamada, and Y. Yamamoto, Phys. Rev. Lett. **85**, 270 (2000).
[15] E. Hiyama, M. Kamimura, T. Motoba, T. Yamada, and Y. Yamamoto, Phys. Rev. C **66**, 024007 (2002).
[16] E. Hiyama, Y. Yamamoto, T. Motoba, and M. Kamimura, Phys. Rev. C **80**, 054321 (2009).
[17] E. Hiyama, M. Kamimura, Y. Yamamoto, and T. Motoba, Phys. Rev. Lett. **104**, 212502 (2010).
[18] R. Wirth, D. Gazda, P. Navratil, A. Calci, J. Langhammer, and R. Roth, Phys. Rev. Lett. **113**, 192502 (2014).
[19] Y. Kanada-En'yo, H. Horiuchi, and A. Ono, Phys. Rev. C **52**, 628 (1995).
[20] M. Isaka, M. Kimura, A. Dote, and A. Ohnishi, Phys. Rev. C **83**, 044323 (2011); **83**, 054304 (2011).
[21] M. Isaka, H. Homma, M. Kimura, A. Dote, and A. Ohnishi, Phys. Rev. C **85**, 034303 (2012).
[22] M. Isaka, M. Kimura, A. Dote, and A. Ohnishi, Phys. Rev. C **87**, 021304(R) (2013).
[23] M. Isaka and M. Kimura, Phys. Rev. C **92**, 044326 (2015).
[24] M. Rayet, Nucl. Phys. A **367**, 381 (1981).
[25] J. Cugnon, A. Lejeune, and H.-J. Schulze, Phys. Rev. C **62**, 064308 (2000).
[26] I. Vidaña, A. Polls, A. Ramos, and H.-J. Schulze, Phys. Rev. C **64**, 044301 (2001).
[27] H.-J. Schulze and T. Rijken, Phys. Rev. C **84**, 035801 (2011).
[28] H.-J. Schulze and T. Rijken, Phys. Rev. C **88**, 024322 (2013).
[29] H.-J. Schulze and E. Hiyama, Phys. Rev. C **90**, 047301 (2014).
[30] X.-R. Zhou, H.-J. Schulze, H. Sagawa, C.-X. Wu, and E.-G. Zhao, Phys. Rev. C **76**, 034312 (2007).
[31] X.-R. Zhou, A. Polls, H.-J. Schulze, and I. Vidaña, Phys. Rev. C **78**, 054306 (2008).
[32] H.-J. Schulze, M. Thi Win, K. Hagino, and H. Sagawa, Prog. Theor. Phys. **123**, 569 (2010).
[33] M.-T. Win and K. Hagino, Phys. Rev. C **78**, 054311 (2008).
[34] M.-T. Win, K. Hagino, and T. Koike, Phys. Rev. C **83**, 014301 (2011).
[35] B.-N. Lu, E.-G. Zhao, and S.-G. Zhou, Phys. Rev. C **84**, 014328 (2011).
[36] B.-N. Lu, E. Hiyama, H. Sagawa, and S.-G. Zhou, Phys. Rev. C **89**, 044307 (2014).
[37] M. Isaka, K. Fukukawa, M. Kimura, E. Hiyama, H. Sagawa, and Y. Yamamoto, Phys. Rev. C **89**, 024310 (2014).
[38] J. M. Yao, Z. P. Li, K. Hagino, M.-T. Win, Y. Zhang, and J. Meng, Nucl. Phys. A **868**, 12 (2011).
[39] H. Mei, K. Hagino, J. M. Yao, and T. Motoba, Phys. Rev. C **90**, 064302 (2014).
[40] W. X. Xue, J. M. Yao, K. Hagino, Z. P. Li, H. Mei, and Y. Tanimura, Phys. Rev. C **91**, 024327 (2015).
[41] H. Mei, K. Hagino, J. M. Yao, and T. Motoba, Phys. Rev. C **93**, 044307 (2016).
[42] H. Mei, K. Hagino, J. M. Yao, and T. Motoba, Phys. Rev. C **91**, 064305 (2015).

[43] H. Mei, K. Hagino, and J. M. Yao, Phys. Rev. C **93**, 011301(R) (2016).
[44] J.-W. Cui, X.-R. Zhou, and H.-J. Schulze, Phys. Rev. C **91**, 054306 (2015).
[45] P. Ring and P. Schuck, *The Nuclear Many-Body Problem* (Springer, Berlin, 1980).
[46] R. Rodriguez-Guzman, J. L. Egido, and L. M. Robledo, Phys. Lett. B **474**, 15 (2000).
[47] P. Bonche, J. Dobaczewski, H. Flocard, P.-H. Henneen, and J. Mayer, Nucl. Phys. A **510**, 466 (1990).
[48] J. M. Yao, Ph.D. thesis, Peking University, 2009 (unpublished).
[49] J. Dobaczewski *et al.*, Comput. Phys. Commun. **180**, 2361 (2009).
[50] M. Bender, K. Rutz, P.-G. Reinhard, and J. A. Maruhn, Eur. Phys. J. A **8**, 59 (2000).
[51] M. Bender, P. Bonche, and P.-H. Heenen, Phys. Rev. C **74**, 024312 (2006).
[52] H. Sagawa, X.-R. Zhou, X.-Z. Zhang, and T. Suzuki, Phys. Rev. C **70**, 054316 (2004).
[53] Y. Zhang, H. Sagawa, D. Yoshino, K. Hagino, and J. Meng, Prog. Theor. Phys. **120**, 129 (2008).
[54] N. Van Giai and H. Sagawa, Phys. Lett. B **106**, 379 (1981).
[55] J. Terasaki, P.-H. Heenen, H. Flocard, and P. Bonche, Nucl. Phys. A **600**, 371 (1996).
[56] National Nuclear Data Center, http://www.nndc.bnl.gov/.
[57] F. Ajzenberg-Selove, Nucl. Phys. A **506**, 1 (1990).
[58] S. Raman, C. W. Nestor, and P. Tikkanen, At. Data Nucl. Data Tables **78**, 1 (2001).
[59] T. Kibedi and R. H. Spear, At. Data Nucl. Data Tables **89**, 77 (2005).
[60] M. Freer, Rep. Prog. Phys. **70**, 2149 (2007).
[61] J.-P. Ebran, E. Khan, T. Niksic, and D. Vretenar, Nature (London) **487**, 341 (2012).
[62] J.-P. Ebran, E. Khan, T. Niksic, and D. Vretenar, Phys. Rev. C **90**, 054329 (2014).
[63] M. Agnello *et al.*, Phys. Lett. B **698**, 219 (2011).
[64] K. Hagino and T. Koike, Phys. Rev. C **84**, 064325 (2011).
[65] K. Hagino, N. W. Lwin, and M. Yamagami, Phys. Rev. C **74**, 017310 (2006).
[66] N. J. Stone, At. Data Nucl. Data Tables **111-112**, 1 (2016).
[67] T. Yamada, K. Ikeda, H. Bandō, and T. Motoba, Prog. Theor. Phys. **71**, 985 (1984).